Asian Journal of Chemistry; Vol. 38, No. 9 (2026), 2356-2362
ASIAN JOURNAL OF CHEMISTRY
https://doi.org/10.14233/ajchem.2026.36354

ZnO Nanoparticle Transition Metal Doping: Effects on Charge Dynamics, Morphological and Magnetic Properties

P.K. RAVI[1], P. RAJESH[1,*], S. KAYASHRINI[1], S. BALA ABIRAMI[2] and R. MOHAMED HISAM[1]

[1]Department of Physics, School of Basic Sciences, Vels Institute of Science, Technology and Advanced Studies, Pallavaram, Chennai-600117, India
[2]Department of Condensed Matter Physics, Saveetha School of Engineering, Saveetha Institute of Medical and Technical Sciences (SIMATS), Chennai-602105, India

*Corresponding author: E-mail: rajesh.ncc5coy@gmail.com

Received: 1 May 2026 *Accepted*: 3 August 2026 *Published online*: 5 September 2026 AJC-22463

ZnO nanoparticles have attracted considerable interest owing to their structural stability, wide band gap, high exciton binding energy and diverse functional characteristics. Their practical performance, particularly in photocatalytic applications, is constrained by rapid electron–hole recombination and limited absorption in the visible region. In the present study, the pristine ZnO (Z1), Cu-doped ZnO (Z2) and Co-doped ZnO (Z3) nanoparticles were synthesized through a controlled co-precipitation route. The prepared materials were characterized by X-ray diffraction (XRD), UV-visible diffuse reflectance spectroscopy (UV-Vis DRS), photoluminescence (PL), Fourier-transform infrared spectroscopy (FT-IR), scanning electron microscopy (SEM), photocatalytic dye degradation and vibrating sample magnetometry (VSM). XRD analysis confirmed the retention of the hexagonal wurtzite ZnO phase after Cu and Co incorporation, accompanied by changes in crystallite characteristics and lattice parameters associated with dopant-induced strain and defect formation. SEM analysis indicated modifications in particle morphology, surface texture and aggregation behaviour upon metal-ion incorporation. The optical characteristics were strongly influenced by doping, with a shift in light absorption toward the visible region and a reduction in charge-carrier recombination, with the Co-doped sample (Z3) exhibiting the most pronounced response. The photocatalytic activity was influenced by the dopant-induced electronic states, which facilitated the separation of photogenerated electron–hole pairs and improved their participation in the photocatalytic process. VSM measurements further established changes in the magnetic response following transition-metal incorporation. The findings establish Cu and Co doping as effective approaches for tailoring the structural, optical, morphological and magnetic characteristics of ZnO nanoparticles, with Co incorporation providing a particularly notable modification of the investigated properties.

Keywords: ZnO nanoparticles, Photocatalysis, Defect states, Charge separation, Visible-light absorption, Magnetic properties.

INTRODUCTION

Zinc oxide (ZnO) is an important II-VI semiconductor with a direct band gap of 3.37 eV and a high exciton binding energy of 60 meV at room temperature. Its chemical stability, low toxicity, abundance and economical synthesis have supported extensive research for electro-optic devices, transparent conducting films, ultraviolet photodetectors, gas sensors, spintronic systems and multifunctional nanomaterials [1-4]. Despite these advantages, the wide band gap restricts visible-light utilization, while rapid electron–hole recombination can limit charge-carrier lifetime and reduce the efficiency of optical and photocatalytic processes [5].

Transition-metal doping provides an effective approach for tailoring the physico-chemical characteristics of ZnO while retaining its hexagonal wurtzite framework [6]. The substitution of Zn^{2+} by transition-metal ions can modify the local lattice environment, introduce strain and defect states, and influence electronic structure, optical absorption, charge-carrier dynamics and magnetic behaviour [7]. Among the other transition metal ions, Cu^{2+} and Co^{2+} are attractive dopants since their ionic dimensions are comparable to Zn^{2+}, favouring substitution at Zn sites under appropriate synthesis conditions [8-10]. Their electronic configurations can introduce additional states within the ZnO electronic structure, providing control over its functional properties.

Although Cu- and Co-doped ZnO have been widely studied individually, comparative investigations using pristine, Cu-doped and Co-doped ZnO synthesized under identical conditions remain limited. Such an approach is important for distinguishing dopant effects from variations arising from synthesis parameters. In this study, pristine ZnO (Z1), Cu-doped ZnO (Z2) and Co-doped ZnO (Z3) nanoparticles were synthesized through a controlled co-precipitation route. The XRD, FTIR, UV-Vis, PL, SEM, photocatalytic dye degradation and VSM were employed to examine their structural, vibrational, optical, morphological, photocatalytic and magnetic characteristics. The comparative assessment establishes the influence of Cu and Co incorporation on the functional properties of ZnO nanoparticles.

EXPERIMENTAL

Starting materials included melamine, sodium hydroxide, copper nitrate ($Cu(NO_3)_2 \cdot 3H_2O$), cobalt nitrate ($Co(NO_3)_2 \cdot 6H_2O$) and zinc acetate dihydrate ($Zn(CH_3COO)_2 \cdot 2H_2O$). All chemicals used were of analytical grade and required no additional purification. Throughout the experiments, deionized water was used.

Synthesis of pure ZnO (Z_1), Cu-doped ZnO (Z_2), Co-doped ZnO (Z_3) nanoparticles: A uniform co-precipitation method with minor doping modifications was used to synthesize the pure ZnO nanoparticles (Z_1), Cu-doped ZnO (Z_2) and Co-doped ZnO (Z_3). Initially, zinc acetate solution (0.2 M, 50 mL) was heated to 85 ºC under continuous stirring, followed by dropwise addition of 0.5 M NaOH until pH 10-11 was attained. The suspension was maintained at 85 ºC for 2 h to promote precursor formation and nucleation. The precipitate was washed repeatedly with ethanol and deionized water, dried at 80 ºC overnight and calcined at 500 ºC for 2 h to obtain pristine ZnO (Z1). Cu- and Co-doped ZnO nanoparticles were synthesized under identical conditions by introducing $Cu(NO_3)_2$ or $Co(NO_3)_2$ into the initial zinc acetate solution to obtain a nominal dopant concentration of 2 wt.%. The resulting precipitates underwent the same pH adjustment, aging, washing, drying and calcination treatments. The final products were designated Z2 (2 wt.% Cu-doped ZnO) and Z3 (2 wt.% Co-doped ZnO), respectively [11].

Characterization: The structural, optical, morphological and magnetic properties of the ZnO-based samples were investigated using standard characterization techniques. FTIR spectra were recorded using a Perkin-Elmer Spectrum Two Fourier Transform Infrared (FTIR) spectrometer in the range of 4000-400 cm^{-1}. XRD patterns were recorded using a Rigaku MiniFlex X-ray diffractometer with Cu*K*α radiation (λ = 1.5406 Å). UV-Vis diffuse reflectance spectra were obtained using a Shimadzu UV-2600i UV-Vis spectrophotometer over the wavelength range of 200-800 nm. Surface morphology and elemental composition were examined using a JEOL JSM-IT200 scanning electron microscope equipped with an EDX detector. Room-temperature magnetic measurements were performed using a Lakeshore 7400 Series vibrating sample magnetometer (VSM). Photoluminescence spectra were recorded using a HORIBA Fluorolog-QM fluorescence spectrometer.

RESULTS AND DISCUSSION

XRD conformation: The XRD pattern of pure ZnO, synthesized using a 0.2 M precursor concentration and 50 mL reaction volume, confirms the formation of single-phase hexagonal wurtzite ZnO, with characteristic reflections at 2θ = 31.7º, 34.3º and 36.1º, assigned to the (100), (002) and (101) planes, respectively (Fig. 1a). The dominant (101) peak indicates a preferred crystal orientation. A significant peak broadening is characteristic of the nanocrystalline structure, with crystallite sizes ranging from 20 to 35 nm [12].

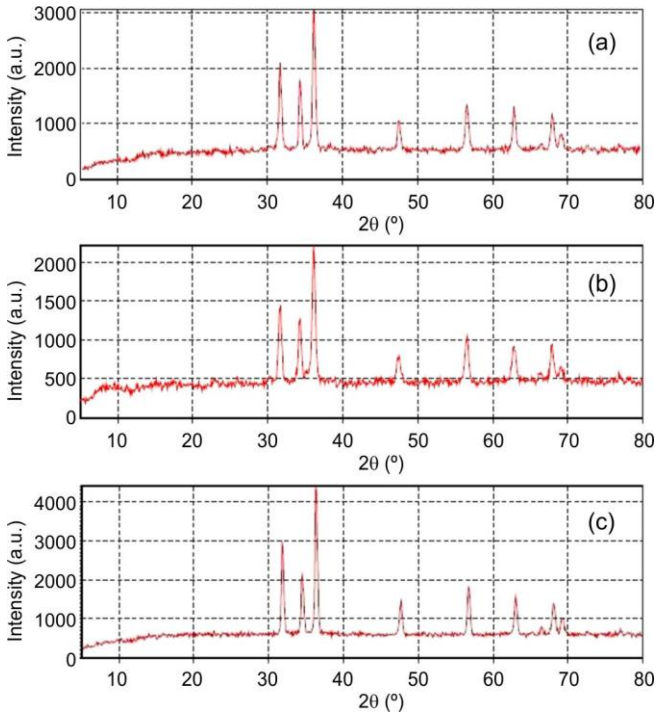

Fig. 1. XRD patterns of (a) pure ZnO, (b) Cu doped ZnO and (c) Co doped ZnO NPs

The XRD pattern of 2% Cu-doped ZnO, prepared using a 0.2 M precursor in a 50 mL reaction volume, exhibits the characteristic reflections of hexagonal wurtzite ZnO at 2θ = 31.6º, 34.3º and 36.1º, corresponding to the (100), (002) and (101) planes, respectively. No additional peaks associated with CuO or Cu_2O are observed, supporting the incorporation of Cu into the ZnO lattice without detect-able formation of a secondary phase [13,14] (Fig. 1b). Compared with pure ZnO, the slight shift of the major reflections toward lower diffraction angles, increased FWHM and reduced peak intensity are consistent with lattice distortion, increased microstrain and a slight decrease in crystallite size following Cu^{2+} incorporation. Similarly, 2% Co-doped ZnO sample also exhibits the characteristic hexagonal wurtzite ZnO reflections at 2θ = 31.83º, 34.50º and 36.33º, corresponding to the (100), (002) and (101) planes, respectively (Fig. 1c). No additional reflections attributable to CoO or Co_3O_4 are detected. These results are consistent with the incorporation of Co^{2+} into the ZnO lattice. Relative to pure ZnO, the diffraction peaks shift toward higher angles, consistent with lattice contraction associated with the smaller ionic radius of Co^{2+} relative to Zn^{2+}. The

decreased FWHM and increased peak intensity following Co doping indicate improved crystallinity and reduced structural disorder.

Photoluminescence (PL) studies: Fig. 2 shows the PL spectra of pure ZnO (Z1), Cu-doped ZnO (Z2) and Co-doped ZnO (Z3) nanoparticles. Pure ZnO exhibits a strong near-band-edge (NBE) ultraviolet emission at approximately 395-400 nm. This emission is attributed to the radiative recombination of free excitons and is associated with the good crystallinity of the ZnO lattice and a relatively low concentration of non-radiative defect centres [15,16]. Following Cu and Co incorporation, the NBE emission intensity decreases and the emission band becomes slightly broader. This behaviour is associated with the introduction of additional defect states by the transition-metal dopants, which can provide pathways for non-radiative charge-carrier recombination.

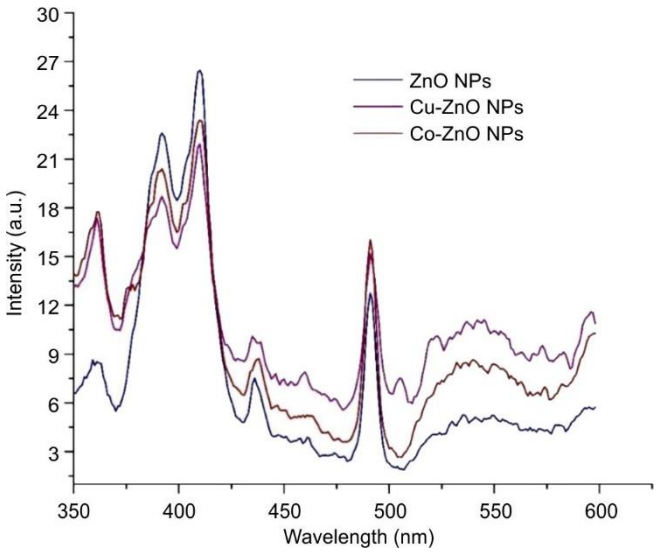

Fig. 2. Photoluminescence spectra of ZnO, Cu-ZnO and Co-ZnO NPs

All samples exhibit a broad visible deep-level (DL) emission extending from approximately 450 to 600 nm. This emission is commonly related to the intrinsic defects such as oxygen vacancies, zinc interstitials, zinc vacancies and surface-associated defect centres [17]. Cu- and Co-doped ZnO exhibit stronger visible emission than pure ZnO, reflecting changes in the defect structure following transition-metal incorporation. Among the investigated samples, Cu-doped ZnO exhibits the highest visible emission intensity, consistent with a more contribution from defect-related luminescence centres. The PL spectra also indicate that Cu and Co incorporation modifies the emission behaviour of ZnO by reducing the NBE emission and increasing the contribution of deep-level emission. The characteristic semiconductor luminescence of ZnO is retained after doping.

SEM studies: SEM was employed to examine the surface morphology of Z1-Z3 samples and to assess the changes associated with Cu and Co incorporation [18]. The pure ZnO sample (Z1) exhibits a relatively homogeneous, quasi-spherical morphology with limited particle aggregation, as shown in Fig. 3. The morphology is characteristic of nanoscale ZnO and reflects relatively uniform particle formation. Following Cu incorporation, the Cu-doped ZnO sample (Z2) exhibits denser agglomeration and noticeably rougher particle surfaces. These morphological changes may be associated with lattice distortion and defect formation accompanying Cu^{2+} incorporation into the ZnO lattice [19]. The Co-doped ZnO sample (Z3) exhibits a more pronounced morphological variation, characterized by increased surface porosity and an irregular appearance. The presence of Co^{2+} may alter the crystal-growth kinetics, resulting in a more heterogeneous particle morphology. The SEM analysis confirms that Cu and Co incorporation modifies the morphology, surface roughness and aggregation of ZnO nanoparticles.

FT-IR structural analysis

Pure ZnO (Z1): The FT-IR spectrum of Z1 (Fig. 4a) shows a strong O–H stretching band at approximately 3465 cm^{-1}, assigned to surface hydroxyl groups associated with the high surface-to-volume ratio of ZnO nanoparticles [20]. The H–O–H bending band at 1630.26 cm^{-1} is attributed to water molecules associated with surface hydroxyl groups [21]. The C–H and C–O bands in the 2925-1450 cm^{-1} region is assigned to small amounts of residual organic species from the synthesis process [22]. The Raman band observed at 432.37 cm^{-1} can be assigned to the E2 (high) phonon mode, which is a characteristic Raman-active mode of the hexagonal wurtzite ZnO lattice. A strong and relatively sharp E2 (high) peak is generally associated with good crystallinity and structural order, whereas phonon broadening and asymmetry can indicate lattice disorder and defects. Therefore, the observed E2 (high) mode at 432.37 cm^{-1} supports the formation of crystalline wurtzite ZnO [23]. The vibrational characteristics clearly reflect a well-structured tetrahedral Zn^{2+}-O^{2-} crystal field, establishing Z1 as a reference point for investigating changes induced by dopants.

Cu-ZnO (Z2): The FT-IR spectrum of Z2 (Fig. 4b) shows strong O–H and H–O–H bands associated with surface hydroxyl groups and adsorbed water following Cu doping [20]. The Zn–O/Cu–O stretching bands at 488.03 and 452.43 cm^{-1}, along with their spectral splitting, are associated with changes in the local bonding environment and lattice distortion after Cu^{2+} incorporation into ZnO [21,22]. Additional bands near 908 and 780 cm^{-1} may be related to Cu–O–H coordination species at the surface [21]. The FT-IR results indicate that Cu doping alters the local bonding environment while retaining the ZnO crystal framework.

Co-ZnO (Z3): The FT-IR spectrum of Z3 sample (Fig. 4c) shows a prominent O–H stretching band at 3435.83 cm^{-1}, associated with surface hydroxyl groups. The metal–oxygen region below 600 cm^{-1} contains bands at 501.41, 463.88 and 435.20 cm^{-1}. The band at 435.20 cm^{-1} can be assigned to the E_2 (high) phonon mode of the wurtzite ZnO lattice, while the additional bands may arise from Co-related vibrational modes and defect-associated lattice vibrations [24]. The splitting of these bands reflects changes in the local lattice environment and Zn–O bonding following Co incorporation. Peaks at 908.97 and 780.55 cm^{-1} are associated with changes in the metal–oxygen vibrational environment; specific assignment to M–OH vibrations requires further spectroscopic evidence [25]. The larger number of metal–oxygen bands in Z3 sample

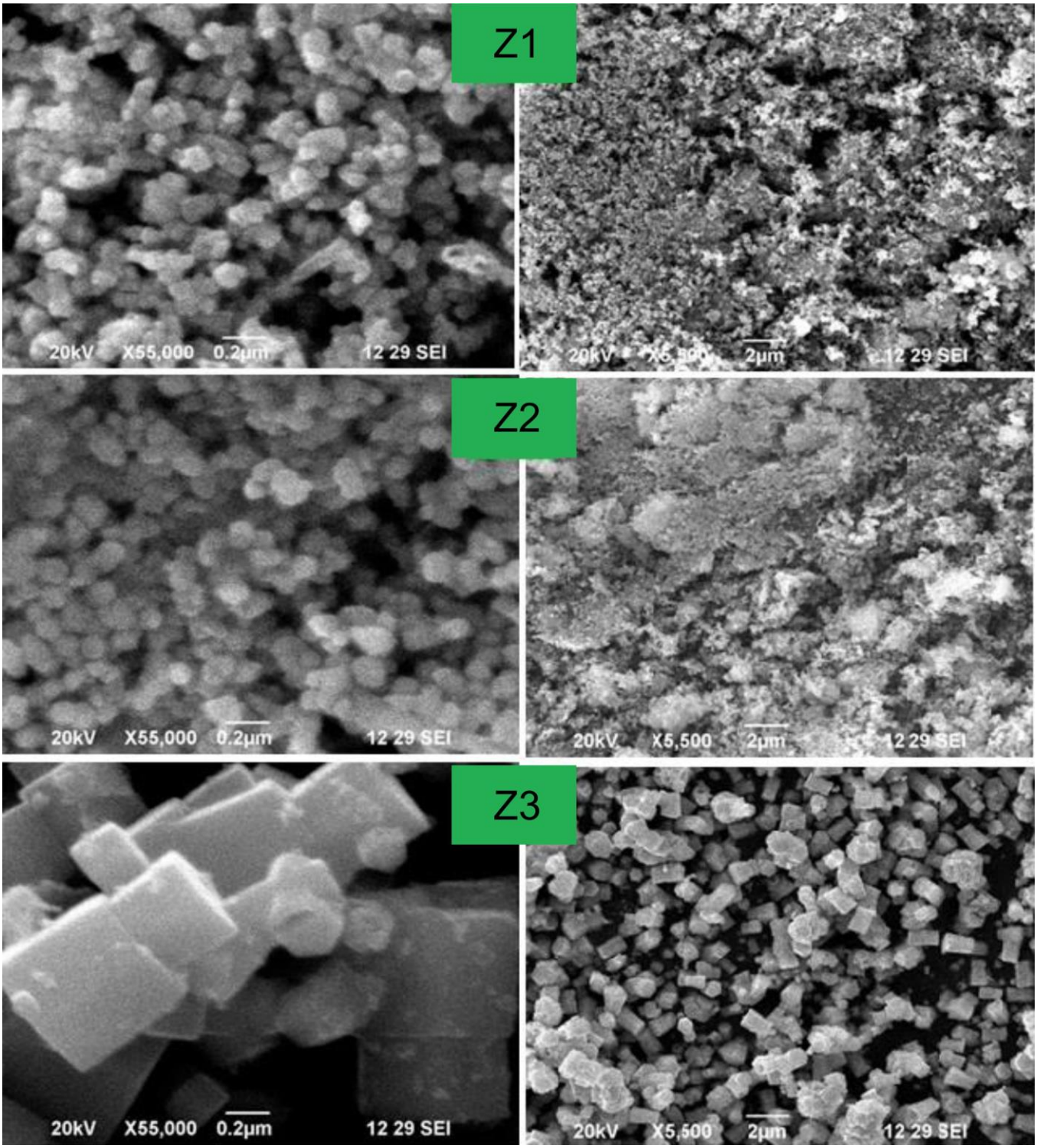

Fig. 3. SEM images of (a) pure ZnO (Z1), (b) Cu doped ZnO (Z2) and (c) Co doped ZnO (Z3) NPs

suggests better structural disorder and a higher contribution of defect-related vibrational features compared with pure ZnO. Thus, Z3 sample consequently exhibits the strongest defect-related structural modification among the investigated samples.

The FT-IR spectra of Z1, Z2 and Z3 samples confirm that the ZnO wurtzite framework is retained after Cu and Co doping. The Z1 sample shows characteristic Zn–O vibrations together with O–H and H–O–H bands related to surface hydroxyl groups and adsorbed water. In Z2, Cu doping causes shifts in the Zn–O vibrational region and introduces additional metal–oxygen bands, reflecting changes in the local bonding environment. Z3 sample exhibits greater splitting of the metal–oxygen bands, consistent with increased lattice distortion following Co incorporation. The spectra indicate that Cu and Co doping alter the local bonding environment of ZnO without disrupting its basic wurtzite structure.

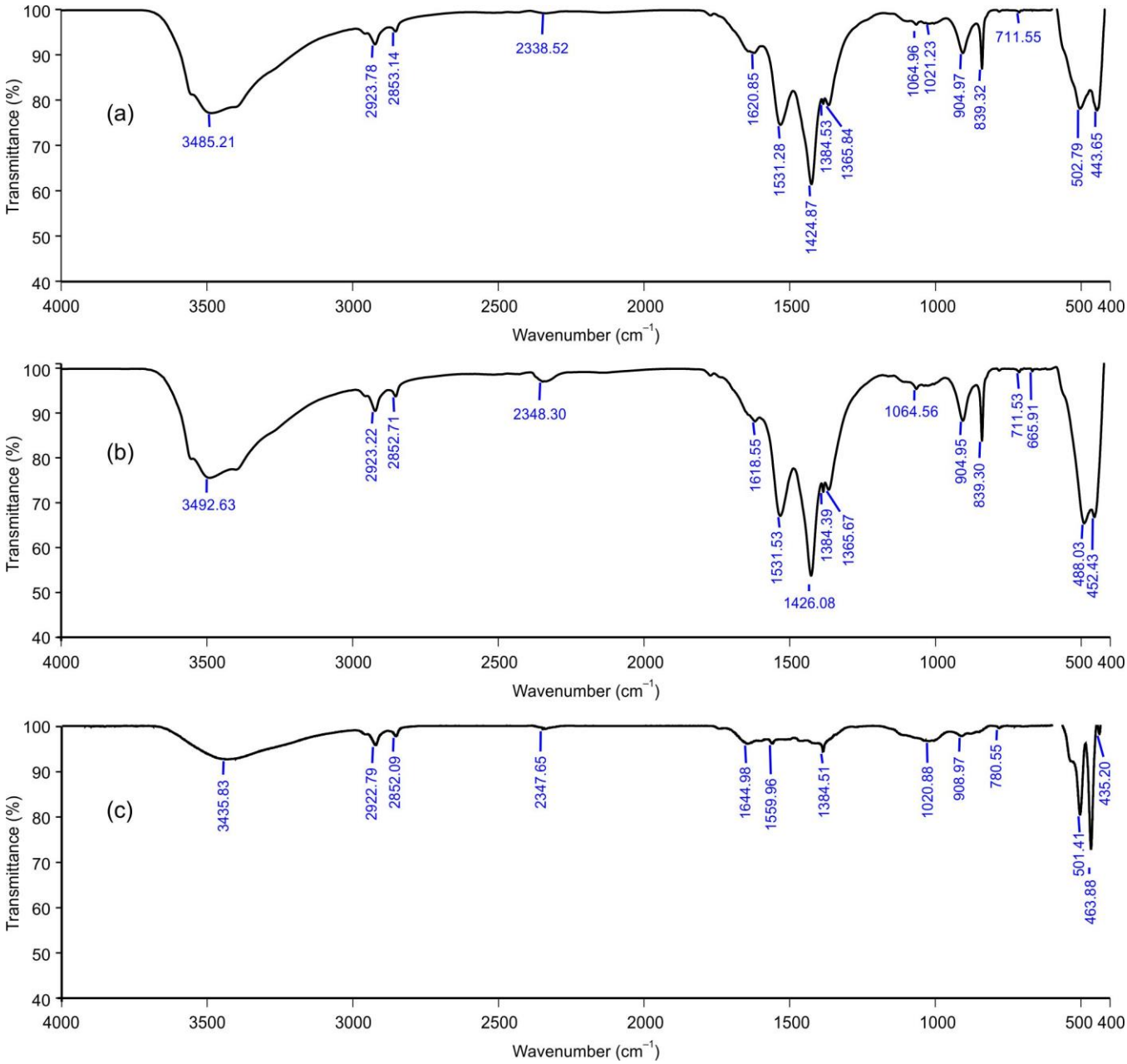

Fig. 4. FTIR spectra of (a) pure ZnO, (b) Cu doped ZnO and (c) Co doped ZnO nanoparticles

VSM analysis: The magnetic properties of the synthesized nanoparticles were investigated using vibrating sample magnetometry (VSM) and the magnetization curves of Z1, Z2 and Z3 are shown in Fig. 5. All samples exhibit nearly linear, non-hysteretic magnetization curves with low coercivity and remanence, consistent with predominantly weak paramagnetic behaviour. This magnetic response is characteristic of nanostructured ZnO-based dilute magnetic semiconductor systems, in which intrinsic defects and dopant-induced changes in the electronic structure contribute to the observed magnetism.

Pure ZnO (Z1) exhibits only a weak magnetic response, consistent with the diamagnetic behaviour generally reported for bulk ZnO. The weak paramagnetic contribution at the nanoscale can be associated with oxygen vacancies, zinc interstitials and surface defects [26]. These defects may generate localized unpaired electrons and contribute to the low magnetic moment observed for Z1. Cu-doped ZnO (Z2) exhibits a noticeable increase in magnetic moment compared with Z1. Incorporation of Cu^{2+} into Zn^{2+} sites can introduce lattice distortion and increase the concentration of oxygen-vacancy-related defects. Such defects can act as centres for exchange interactions between localized Cu spins. Defect-mediated magnetic interactions and bound magnetic polaron (BMP) formation have been proposed for transition-metal-doped ZnO systems. The possible presence of Cu^{+}/Cu^{2+} mixed-valence states may further contribute to these interactions [27]. The higher magnetic moment of Z2 sample is consistent with Cu incorporation and the associated increase in defect concentration. Among the three samples, Co-doped ZnO (Z3) exhibits

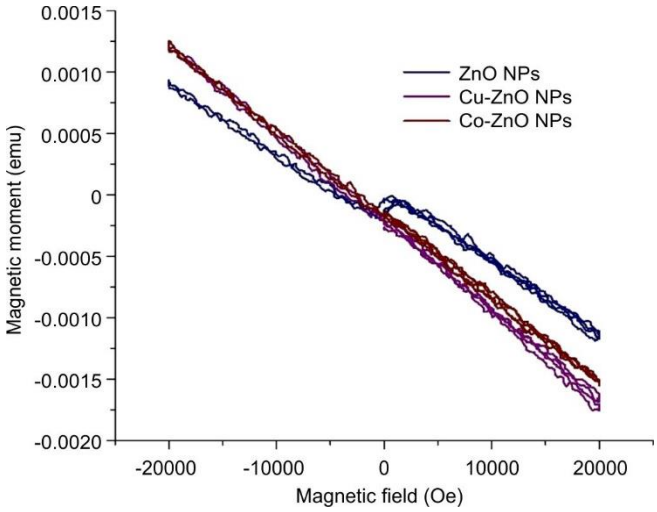

Fig. 5. VSM analysis of ZnO, Cu-ZnO and Co-ZnO nanoparticles

the strongest magnetic response. Co^{2+} ions possess partially filled 3*d*-orbitals and introduce localized magnetic moments into the ZnO matrix. Their incorporation can modify spin–spin and spin–orbit interactions and promote defect formation. The combined contribution of Co^{2+} ions and defect sites can account for the enhanced room-temperature paramagnetic response observed for Z3. The substantially higher magnetic moment of Z3 compared with Z1 and Z2 is consistent with the stronger magnetic contribution from Co incorporation and the associated defect structure.

The systematic variation in magnetic response from Z1 to Z3 samples reflects changes in the electronic structure and defect chemistry of ZnO following transition-metal incorporation [28]. Cu and Co doping enhance the magnetic response through dopant-related defects and oxygen vacancy-mediated interactions [29]. Although all samples exhibit weak paramagnetic behaviour, the progressive increase in magnetic moment demonstrates that transition-metal incorporation provides a means of modifying the magnetic properties of ZnO nanoparticles [30]. These characteristics support the potential use of doped ZnO as a multifunctional oxide semiconductor for applications requiring controlled magnetic and electronic properties.

Conclusion

The systematic synthesis and characterization of pure and transition-metal-doped ZnO nanoparticles establish the effects of controlled Cu^{2+} and Co^{2+} incorporation on their structural, morphological, optical and magnetic properties. XRD and FTIR analyses confirm retention of the hexagonal wurtzite structure, accompanied by lattice strain and changes in the local bonding environment after doping. SEM analysis shows changes in particle morphology, surface roughness and aggregation, which can modify the accessible surface sites and surface interactions. Optical measurements show a progressive change in properties from Z1 to Z2 and Z3 samples. Cu doping introduces additional defect states, while Co doping results in the stronger deep-level emission and a higher modification of the charge-carrier recombination behaviour. Z3 sample exhibits enhanced visible-light absorption, lower PL intensity and improved charge-carrier separation relative to the other samples. VSM measurements show an enhanced weak paramagnetic response after Cu and Co incorporation, reflecting changes in the defect structure and electronic environment of ZnO. Among the investigated materials, Z2 sample provides an intermediate response, whereas Z3 sample exhibits the most pronounced changes in optical and magnetic properties. The results support controlled transition-metal incorporation as a useful approach for tailoring ZnO nanoparticles for optoelectronic, photocatalytic and other functional applications.

CONFLICT OF INTEREST

The authors declare that there is no conflict of interests regarding the publication of this article.

DECLARATION OF AI-ASSISTED TECHNOLOGIES

During the preparation of this manuscript, the authors used an AI-assisted tool(s) to improve the language and no data, results or scientific conclusions were generated by AI. All analyses, interpretations and conclusions are the authors' own. The authors reviewed and edited the content and take full responsibility for the published work.

REFERENCES

1. C.B. Ong, L.Y. Ng and A.W. Mohammad, *Renew. Sustain. Energy Rev.*, **81**, 536 (2018); https://doi.org/10.1016/j.rser.2017.08.020
2. A.P. Bhirud, S.D. Sathaye, R.P. Waichal, S. Park, B.B. Kale and C.R. Holkar, *Mater. Sci. Semicond. Process.*, **39**, 80 (2015); https://doi.org/10.1016/j.mssp.2015.04.043
3. S. Kumar, F. Ahmed, N. Ahmad, N.M. Shaalan, R. Kumar, A. Alshoaibi, N. Arshi, S. Dalela, F. Sayeed and K. Kumari, *Materials*, **15**, 8184 (2022); https://doi.org/10.3390/ma15228184
4. Z. Ma, H. Cai, L. Yu and J. Chen, *Materials*, **12**, 2100 (2019); https://doi.org/10.3390/ma12132100
5. M. Norek, *Curr. Appl. Phys.*, **19**, 867 (2019); https://doi.org/10.1016/j.cap.2019.05.006
6. V.M.A. Lage, C. Rodríguez-Fernández, F.S. Vieira, R.T. da Silva, M.I.B. Bernardi, M.M. de Lima Jr., A. Cantarero and H.B. de Carvalho, *Acta Mater.*, **259**, 119258 (2023); https://doi.org/10.1016/j.actamat.2023.119258
7. P. Kaur, Rahul, S. Kaur, K. Kriti, D. Arora, K. Asokan and D.P. Singh, *Materials Today: Proc.*, **26**, 3436 (2020); https://doi.org/10.1016/j.matpr.2019.12.001
8. N. Akbar, M. Shahid, S. Bano and S. Mahmood, *AMB Express*, **11**, 172 (2021); https://doi.org/10.1186/s13568-021-01261-1
9. A. Sedky, N. Afify, A. Almohammedi, E.M.M. Ibrahim and A.M. Ali, *Opt. Quantum Electron.*, **55**, 456 (2023); https://doi.org/10.1007/s11082-023-04718-8
10. U. Chaitra, H. Nagabhushana, K.S. Anantharaju, S.C. Sharma and S.C. Prashantha, *J. Magn. Magn. Mater.*, **529**, 167870 (2021); https://doi.org/10.1016/j.jmmm.2021.167870
11. R. Saravanan, S. Karthikeyan, V.K. Gupta, G. Sekaran, V. Narayanan and A. Stephen, *Mater. Sci. Eng. C*, **33**, 91 (2013); https://doi.org/10.1016/j.msec.2012.08.011
12. A. Sedky, N. Afify, A. Almohammedi, E.M.M. Ibrahim and A.M. Ali, *Opt. Quantum Electron.*, **55**, 456 (2023); https://doi.org/10.1007/s11082-023-04718-8
13. A.P. Bhirud, S.D. Sathaye, R.P. Waichal, S. Park, B.B. Kale and C.R. Holkar, *Mater. Sci. Semicond. Process.*, **39**, 80 (2015); https://doi.org/10.1016/j.mssp.2015.04.043
14. S. Kumar, F. Ahmed, N. Ahmad, N.M. Shaalan, R. Kumar, A. Alshoaibi, N. Arshi, S. Dalela, F. Sayeed and K. Kumari, *Materials*, **15**, 8184 (2022); https://doi.org/10.3390/ma15228184

15. Z. Ma, H. Cai, L. Yu and J. Chen, *Materials*, **12**, 2100 (2019); https://doi.org/10.3390/ma12132100
16. S.A. Ansari and M.H. Cho, *J. Ind. Eng. Chem.*, **82**, 97 (2020); https://doi.org/10.1016/j.jiec.2019.10.024
17. L. Xu, H. Wu and D. Tan, *Mater. Chem. Phys.*, **305**, 127917 (2023); https://doi.org/10.1016/j.matchemphys.2023.127917
18. J. Zhang, H. Chen, G. Xiao, M. Yi, Z. Chen, J. Zhang, X. Shang and C. Xu, *Ceram. Int.*, **48**, 8097 (2022); https://doi.org/10.1016/j.ceramint.2021.12.011
19. H. Noei, H. Qiu, Y. Wang, E. Löffler, C. Wöll and M. Muhler, *Phys. Chem. Chem. Phys.*, **10**, 7092 (2008); https://doi.org/10.1039/b811029h
20. S. Alamdari, M.S. Ghamsari, C. Lee, W. Han, H.H. Park, M.J. Tafreshi, H. Afarideh and M.H.M. Ara, *Appl. Sci.*, **10**, 3620 (2020); https://doi.org/10.3390/app10103620
21. W. Muhammad, N. Ullah, M. Haroon and B. H. Abbasi, *RSC Adv.*, **9**, 29541 (2019); https://doi.org/10.1039/C9RA04424H
22. N. Akbar, M. Shahid, S. Bano and S. Mahmood, *AMB Express*, **11**, 104 (2021); https://doi.org/10.1186/s13568-021-01261-1
23. R.L. de Sousa e Silva and A. Franco Jr., *Mater. Sci. Semicond. Process.*, **119**, 105227 (2020); https://doi.org/10.1016/j.mssp.2020.105227
24. A. Chanda, S. Gupta, M. Vasundhara, S. R. Joshi, G. R. Mutta and J. Singh, *RSC Adv.*, **7**, 50527 (2017); https://doi.org/10.1039/C7RA08458G
25. A. Safeen, K. Safeen, M. Shafique, Y. Iqbal, N. Ahmed, M.A. Rauf Khan, G. Asghar, K. Althubeiti, S. Al Otaibi, G. Ali, W.H. Shah and R. Khan, *RSC Adv.*, **12**, 11923 (2022); https://doi.org/10.1039/D2RA01798A
26. Q. Xu, S. Zhou and H. Schmidt, *J. Alloys Comp.*, **487**, 665 (2009); https://doi.org/10.1016/j.jallcom.2009.08.033
27. N. Ali, B. Singh, Z.A. Khan, V.A.R. Vijaya, K. Tarafder and S. Ghosh, *Sci. Rep.*, **9**, 2461 (2019); https://doi.org/10.1038/s41598-019-39660-x
28. R. Bhardwaj, A. Bharti, J. P. Singh, K. H. Chae and N. Goyal, *Nanoscale Adv.*, **2**, 4450 (2020); https://doi.org/10.1039/D0NA00499E
29. Y. Zong, Y. Sun, S. Meng, Y. Wang, H. Xing, X. Li and X. Zheng, *RSC Adv.*, **9**, 23012 (2019); https://doi.org/10.1039/C9RA03620B
30. Q.-Y. Xu, X.-H. Zheng, and Y.-P. Gong, *Chinese Phys. B*, **19**, 077501 (2010); https://doi.org/10.1088/1674-1056/19/7/077501